

BUDHIES I: characterizing the environments in and around two clusters at $z \simeq 0.2$

Yara L. Jaffé^{1,2,3*}, Bianca M. Poggianti², Marc A. W. Verheijen³, Boris Z. Deshev^{3,4},
Jacqueline H. van Gorkom⁵

¹*Department of Astronomy, Universidad de Concepción, Casilla 160-C, Concepción, Chile*

²*INAF - Osservatorio Astronomico di Padova, vicolo dell' Osservatorio 5, I-35122 Padova, Italy*

³*University of Groningen, Kapteyn Astronomical Institute, Landleven 12, 9747 AD, Groningen, The Netherlands*

⁴*Tartu Observatory, Tõravere, 61602, Estonia*

⁵*Department of Astronomy, Columbia University, Mail Code 5246, 550 W 120th Street, New York, NY 10027, USA*

20 November 2021

ABSTRACT

We present the optical spectroscopy for the Blind Ultra Deep HI Environmental Survey (BUDHIES). With the Westerbork Synthesis Radio Telescope, BUDHIES has detected HI in over 150 galaxies in and around two Abell clusters at $z \simeq 0.2$. With the aim of characterizing the environments of the HI-detected galaxies, we obtained multi-fiber spectroscopy with the William Herschel Telescope. In this paper, we describe the spectroscopic observations, report redshifts and EW[OII] measurements for ~ 600 galaxies, and perform an environmental analysis. In particular, we present cluster velocity dispersion measurements for 5 clusters and groups in the BUDHIES volume, as well as a detailed substructure analysis.

Key words: Galaxies:clusters:general – Galaxies:clusters:inividual (Abell 963 and Abell 2192) – Galaxies:evolution

1 INTRODUCTION

Rich clusters of galaxies, in relation to the large scale structure in which they are embedded, offer a unique laboratory to study the effects of global and local environments on the properties of their constituent galaxies. Evidence has accumulated that the star formation activity, as well as galaxy morphology strongly depend on the environment in which galaxies are located. This is well exemplified by the morphology-density relation (Dressler 1980), that shows that early-type galaxies are more frequent in regions with high local density (the number of galaxies per unit projected area, or volume), while spirals dominate the low-density regions.

The evolution of galaxy properties in clusters is strong, even in the last few Gyrs: the fraction of blue galaxies in clusters was higher in the past (Butcher-Oemler B-O effect, Butcher & Oemler 1978), and the relative number of S0 galaxies increases with time, at the expense of the spiral population (Dressler et al. 1997; van Dokkum et al. 1998; Fasano et al. 2000; Desai et al. 2007). Similar trends are now known to take place also in the field (Bell 2007; Oesch

et al. 2010), where the relative numbers of red, passively evolving, early-type galaxies increases with time.

Recent large surveys (SDSS, 2dF, Lewis et al. 2002; Gómez et al. 2003; Haines et al. 2007; Mahajan et al. 2012) and studies of groups, cluster outskirts and filaments (e.g. Treu et al. 2003; Wilman et al. 2009; Fadda et al. 2008; Porter et al. 2008; Roychowdhury et al. 2012) have shown that the environmental dependencies extend to the lowest density environments. It is now thought that galaxies may be “preprocessed” before they fall into clusters, i.e. environmentally driven evolution occurs in lower density environments. A remaining question is where and how does this happen.

Further clues (or perhaps questions) come from the structure formation scenario of Λ cold dark matter (Λ CDM) cosmology, that predicts that many galaxies have undergone the transition from field to cluster environments since $z \lesssim 1$ (De Lucia et al. 2012). In fact, there is an ongoing debate on whether it is the cluster environment that drives galaxy evolution and transforms galaxies (nurture), the field population that accretes onto clusters and that evolves with cosmic time (nature), or both (e.g. Poggianti et al. 1999; Kauffmann et al. 1999; Kodama & Bower 2001; Ellingson

* E-mail: yara.jaffe@astro-udec.cl

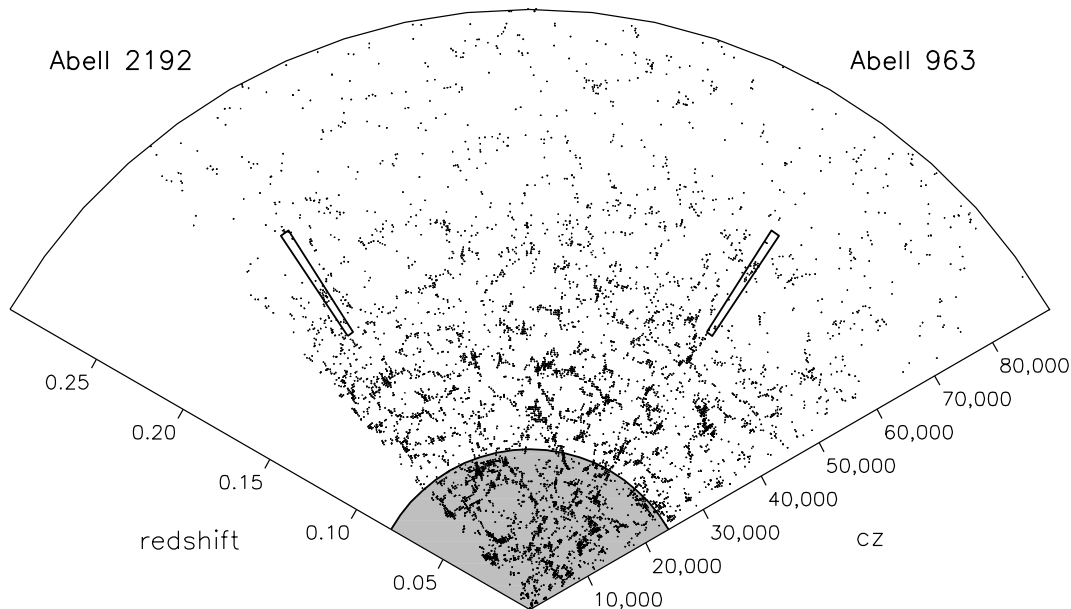


Figure 1. A redshift pie-diagram. Dots represent galaxies with optical redshifts from the SDSS. The elongated rectangles indicate the two volumes that have been surveyed with the WSRT (at $0.164 \leq z \leq 0.224$). At these redshifts, the large scale structure becomes sparsely sampled by the SDSS. The lower light-gray “pie” indicates the highest redshift ($z = 0.08$) out to which HI imaging data existed before. Note that the HIPASS survey (Meyer et al. 2004) does not extend beyond $cz=12,000 \text{ km s}^{-1}$ while the Alfalfa survey (Giovannelli et al. 2005) with the Arecibo telescope is restricted to $z \lesssim 0.06$.

et al. 2001; Desai et al. 2007; Bolzonella et al. 2010; Vulcani et al. 2010; Jaffé et al. 2011).

A crucial tracer of galaxy evolution is the neutral atomic hydrogen gas from which the stars are formed. HI is a sensitive tracer of different environmental processes, in particular of tidal interactions and ram-pressure stripping. Observational evidence (e.g. Cayatte et al. 1990; Bravo-Alfaro et al. 2000, 2001; Poggianti & van Gorkom 2001; Kenney et al. 2004; Crowl et al. 2005; Chung et al. 2007, 2009; Abramson et al. 2011; Scott et al. 2010, 2012) have suggested that the HI gas is disturbed and eventually truncated and exhausted in the cores of galaxy clusters, where the intra-cluster medium is denser. This is further supported by simulations (see Roediger 2009, for a review), that have suggested that the cause of the distortion is ram pressure stripping and gravitational interaction with the cluster (e.g. Vollmer 2003; Tonnesen & Bryan 2009; Kapferer et al. 2009, and references therein). Moreover, observational studies have found that HI distributions showing interaction and gas stripping are particularly common in galaxy groups (e.g. Verdes-Montenegro et al. 2001; van der Hulst 1979; Kern et al. 2008; Freeland et al. 2009; Hibbard et al. 2001, and references therein). In particular, Verdes-Montenegro et al. (2001) showed that the HI content of compact groups is a decreasing function of their compactness.

Due to technological limitations, studies of the neutral atomic hydrogen gas content in galaxies have been mostly carried out in the local Universe ($z < 0.08$). The main impediments for HI surveys to be carried at higher redshifts are the necessarily long integration times and the occurrence of man-made interference at those frequencies.

With the aim of understanding where, how, and why

star-forming spiral galaxies get transformed into passive early-type galaxies, we have embarked on a Blind Ultra Deep HI Environmental Survey (BUDHIES) with the Westerbork Synthesis Radio telescope (WSRT). We refer to Verheijen et al. (2007) and Deshev et al. (in preparation) for technical details on the HI survey. The strategy has been to study in detail two galaxy clusters, at $z \simeq 0.2$, and the large scale structure around them. The surveyed clusters Abell 2192 and Abell 963 (A2192 and A963 from now on) are very different. A963 is a massive lensing cluster with an unusually large fraction of blue galaxies (Butcher et al. 1983). A2192 is a less massive cluster with significant substructure (Jaffé et al. 2012). Our aim is to identify the physical mechanisms (e.g. tidal interactions, gas stripping, etc) that govern these transformations. The unique aspect of our study is that we have accurate measurements of the HI gas content. While much optical work has been done on clusters at intermediate redshifts ($z=0.4$ and above), and much HI work on nearby clusters ($z < 0.08$), our study is the first where optical properties and gas content are combined at a redshift where evolutionary effects begin to show.

We have surveyed the two clusters with several instruments in different wavelengths. At the core of the survey are the ultra-deep HI observations, carried out at the WSRT, that yielded over 150 detections of galaxies with optical counterparts at $z \simeq 0.2$. To assess the environments of the HI-detections, we have pursued optical spectroscopic observations, which are the subject of this paper.

Our final goal is to relate the HI characteristics of the galaxies to their environment (see first results in Jaffé et al. 2012), as well as to the galaxy luminosities, stellar masses, morphologies, star formation rates and histories. In this pa-

per, we describe the spectroscopic observations carried out at the William Herschel Telescope (WHT), and the characterization of environment. We leave the rest of the analysis for a series of upcoming papers.

In Section 2 we summarize the survey strategy and the multi-wavelength data collected to date. In Section 3 we present the spectroscopic observations and the data reduction, the redshift and EW[OII] measurements, and the spectroscopic completeness. In Section 4 we identify the clusters and groups in the sample and compute velocity dispersion, R_{200} and cluster membership. We then inspect the clusters thoroughly for substructure in Section 5, and summarize the main characteristics of each of the identified cluster/groups in Section 6. Finally, we present our conclusions in Section 7.

Throughout this paper, we use Vega magnitudes and assume a “concordance” Λ CDM cosmology with $\Omega_M = 0.3$, $\Omega_\Lambda = 0.7$, and $H_0 = 70 \text{ km s}^{-1} \text{ Mpc}^{-1}$, unless otherwise stated.

2 THE BUDHIES PROJECT

The WSRT deep environmental survey targeted two clusters at $z \simeq 0.2$, as well as the large scale structure around them. The surveyed clusters, A2192 and A963, are very distinct. A963 at $z=0.206$ is a massive lensing B-O cluster with an unusually large fraction of blue galaxies ($f_B=0.19$, Butcher et al. 1983), and a total X-ray luminosity of $L_X \simeq 3.4 \pm 1 \times 10^{44} h^{-2} \text{ ergs/s}$ (Allen et al. 2003). A2192 at $z=0.188$ is a less massive cluster in the process of forming, with a high degree of substructure (Jaffé et al. 2012). It has a velocity dispersion of 653 km s^{-1} and is barely detected in X-rays ($L_X \simeq 7 \times 10^{43} h^{-2} \text{ erg/s}$; Voges et al. 1999). With the assumed cosmology, the spatial scales at the distances of A963 and A2192 are 3.4 and 3.1 kpc arcsec $^{-1}$ respectively.

After integrating for 117×12^h on A963 and 76×12^h on A2192 with the WSRT, more than 150 galaxies were detected and imaged in HI. The observations span a redshift range of 0.164 – 0.224, a luminosity distance of 0.79 – 1.11 Gpc, and a lookback time interval of 2.04 – 2.68 Gyr. The results of a pilot study are presented in Verheijen et al. (2007). In short, this recently completed 4-year long-term Large Programme focused on two (single-pointing) volumes, each containing an Abell cluster of galaxies, as well as foreground and/or background voids, sampling the broadest range of cosmic environments. The depth of the WSRT observations allow a solid detection of a minimum HI mass of $2 \times 10^9 M_\odot$ (5 sigma), assuming a typical width of 100 km s^{-1} . It should be noted that the galaxy clusters only occupy $\sim 4\%$ of the surveyed volumes while the entire combined volume that has been blindly surveyed with the WSRT is $\sim 73,000 \text{ Mpc}^3$, equivalent to the volume of the Local Universe within a distance of 26 Mpc.

In addition to the HI data, we have obtained near and far UV imaging with GALEX (Montero-Castaño et al. in preparation); 3.6, 4.5, 5.6, 8, 24 and 70 micron imaging with Spitzer (Cybulski et al. in preparation); Herschel imaging (with SPIRE and PACS, Yun et al. in preparation); as well as 36 spectra with the Wisconsin Indiana Yale NOAO (WIYN) Telescope in the field of A2192. Finally, we also obtained B - and R -band imaging with the Isaac Newton Telescope (INT) in both clusters. These observations over

a 1 square degree field were carried out under significantly better seeing conditions, and are much deeper than the available Sloan Digital Sky Survey (SDSS) photometry.

Figure 1 shows a redshift pie-diagram from available SDSS redshifts, showing the location of our surveyed clusters at $z \simeq 0.2$ and highlighting the depth of the HI survey. This diagram already shows overdensities at the studied redshifts but it is evident that additional spectroscopy is needed to define the structures. In addition to the SDSS and WIYN redshifts, we also have 89 redshifts in the very centre of A963 from Lavery & Henry (1994, and private communication), as well as 111 redshifts from Oliver Czoske (private communication) in the same field. However, the redshifts from Lavery & Henry (1994) were used cautiously, as they suffer from large uncertainties.

In the following section we present optical spectroscopy of a large number of galaxies in the two volumes, obtained at the William Herschel Telescope (WHT).

3 OPTICAL SPECTROSCOPY

3.1 Target selection

To design the spectroscopic observations, we made use of the B - and R -band magnitudes, the astrometry, and the galaxy-star separation from the INT photometry, as well as the HI-detection information and the available redshifts. Our selection and prioritization criteria are summarized in the following:

(i) **Type of object:** the galaxy-star separation index (as given by *SExtractor*) in either the B - or the R -band was ≤ 0.3 , in order to clean the sample from objects that are not galaxy-like.

(ii) **Location in the colour-magnitude diagram (CMD):** For each field we created CMDs showing R versus $B - R$ (see Figure 2) for all the sources detected in the photometry that were classified as galaxies (c.f. bullet point (i)). We selected galaxies within the black solid boxes shown in the CMDs of Figure 2 and included fainter HI-detected galaxies (up to $R = 20.5$). This was done partially to confirm clear optical counterparts of fainter HI-detections. The magnitude limits for each field are listed in Table 2. Figure 2 shows that the red sequence is well-defined in both clusters. The figure also shows that the vast majority of HI-detected galaxies are located in the so-called “blue cloud”.

(iii) **Area in the sky:** Although fibers can be positioned over a field of 1 degree diameter, we only selected galaxies inside a radius of 25 arcmin (centered on the pointings of the HI observations), as it is the radius within which vignetting is not dramatically strong. The spatial distribution of the targeted galaxies (red circles) and the field of view of the WSRT and WHT are shown in Figure 3.

(iv) **Prioritizing the fiber allocation:** When allocating fibers to objects, we gave the top priority to HI-detected galaxies, lower priority to other targeted galaxies, and the lowest priority to galaxies that already had redshifts from the literature¹ in the range of the HI survey (see Table 1). Furthermore, when the literature redshifts were

¹ Whenever we refer to “literature redshifts” we are referring to SDSS, WIYN, Lavery & Henry and Czoske (see Section 2).

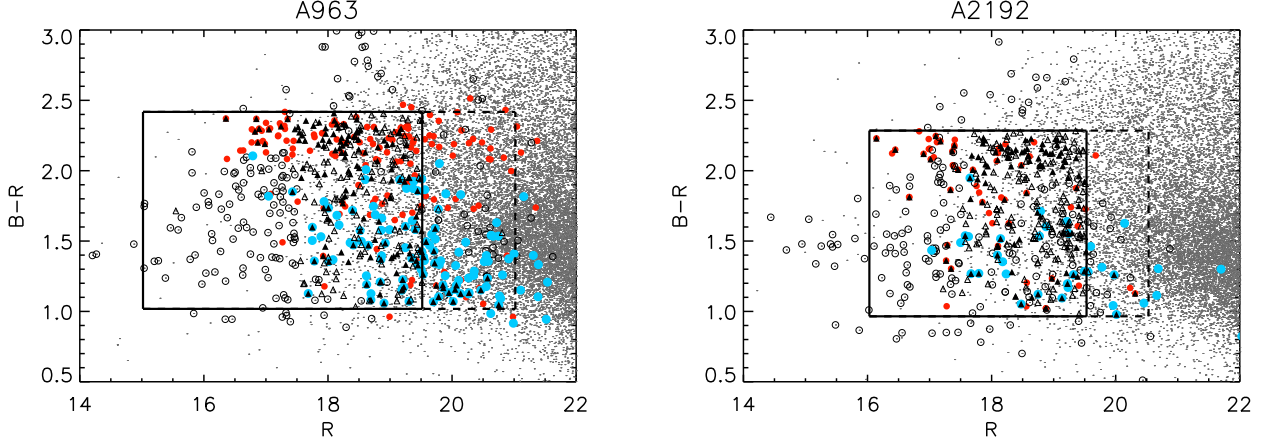


Figure 2. The CMDs of A963 (left) and A2192 (right). All galaxies in the SDSS photometric catalogs and in our INT images are plotted in small gray dots. The red filled circles indicate galaxies with literature redshifts that lie inside the HI redshift range ($0.164 \leq z \leq 0.224$), whilst the black open circles are those with literature redshifts outside this range. The bigger blue filled circles highlight the HI-detected galaxies. Solid triangles correspond to new WHT redshifts inside the HI redshift range, and open triangles are those with WHT redshifts outside the range. In each case, the solid box delimits the region containing the galaxies targeted for spectroscopy, and the extended dashed area shows the fainter range in which only galaxies with HI detections were targeted.

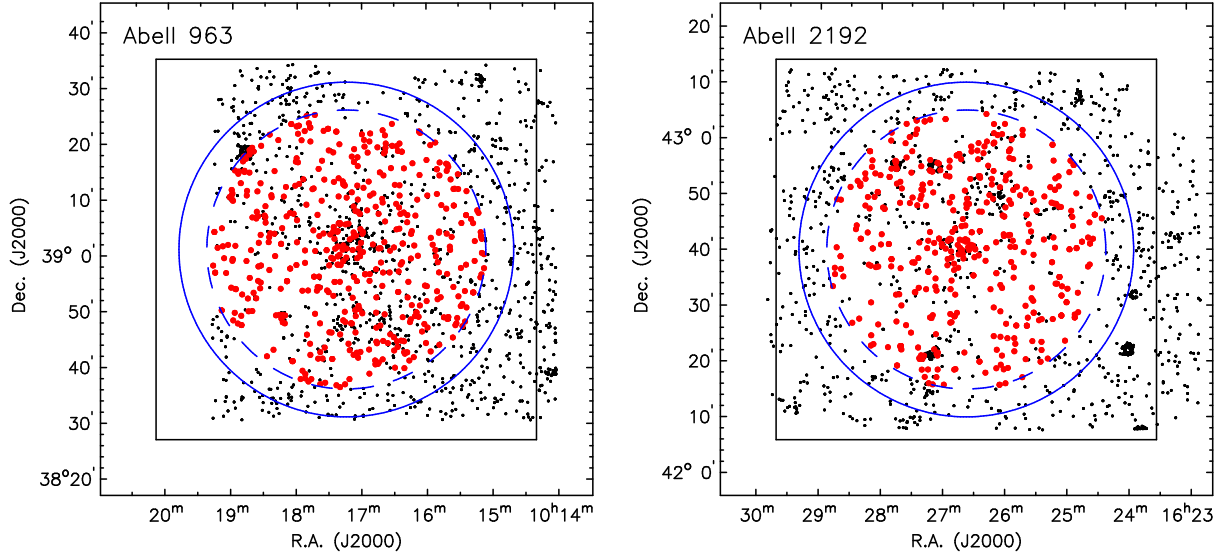


Figure 3. The distribution of targeted (black points) and observed (red filled circles) galaxies in A963 (left) and A2192 (right). The black square represents the area within $68 \times 68 \text{ arcmin}^2$ of the WSRT pointings. The bigger circle ($30'$ radius) encloses the field of view of WHT, whilst the smaller dashed circle ($25'$ radius) shows the unvignetted area.

outside the cluster redshift range (open black circles in Figure 2), we explicitly rejected the galaxies.

3.2 Observations and data reduction

The spectroscopic observations were made using the AutoFib2+WYFFOS (AF2) wide-field, multi-fiber spectrograph mounted on the 4.2m WHT in La Palma. AF2 contains 150 science fibers (of 1.6 arcsec diameter and 26 metres in length), and 10 fiducial bundles for acquisition and guiding. At the prime focus, the fibers are placed onto a field plate by a robot positioner at user-defined sky coordinates.

Object light is transmitted along the fibers to the spectrograph.

We used the R600B grating with the 2-chip EEV 4300×4300 mosaic that counts with 13.5μ pixels. Using a 2×3 binning of the CCD pixels, we obtained a spectral resolution of $\sim 4\text{\AA}$ FWHM (depending on the location on the CCD). The spectra were centered on a wavelength of $\sim 4900\text{\AA}$ and covered the range $\sim 3900 - 6900\text{\AA}$. In this range, galaxies at the targeted redshift showed spectral features from the Ca H&K lines, and the [OII] line in the blue, up to NaD in the red (see Figure 4). We used He and Ne lamp exposures for wavelength calibration.

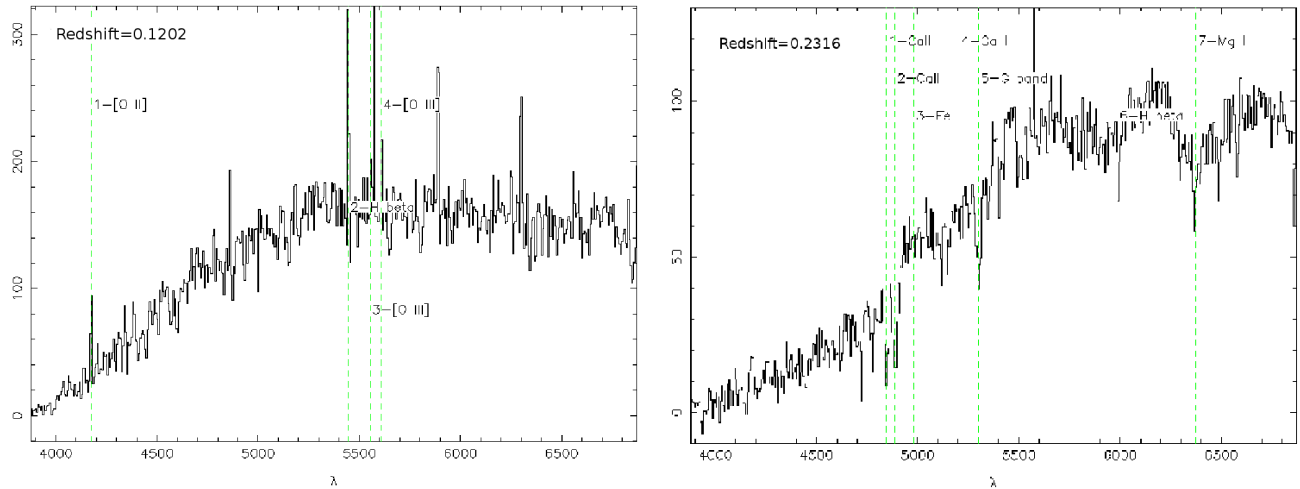


Figure 4. Example of the extracted, calibrated and sky-subtracted spectra for a galaxy with strong [OII] emission, as well as some absorption features (left) and an absorption-line galaxy (right). The wavelength (λ) is expressed in Å and the flux (vertical axes) in arbitrary units. Green vertical lines indicate the main lines (such as [OII] emission or the Ca H&K absorption lines) from which the redshift was calculated. The measured redshift in each case is also indicated at the top left corner of each spectra.

Table 2. Magnitude and colour limits for spectroscopic target selection. The colours cuts were applied to all samples, and the magnitude limits are those highlighted with boldface (see also the red boxes in Figure 2). We split the galaxy sample into “bright”, “faint” and “fainter HI-galaxies”, to produce configurations of the same exposure time, and maintain the signal-to-noise above 10. The bright configurations were observed for ≥ 1 hour, whilst the faint configurations (including the fainter HI-galaxies) were observed for ≥ 3 hours.

Field	Bright sample	Faint sample	Fainter HI-galaxies	Colour constraints
Abell 963	$15.0 < R < 18.5$	$18.5 < R < 19.5$	$19.5 < R < 21.0$	$0.98 < B - R < 2.38$
Abell 2192	$16.0 < R < 18.5$	$18.5 < R < 19.5$	$19.5 < R < 20.5$	$0.92 < B - R < 2.24$

Table 1. For each field the table lists: the number of galaxies with redshifts available from the literature in the two surveyed fields (within $0.164 \leq z \leq 0.224$), number of HI-detected galaxies, number of galaxies targeted for WHT spectroscopy (fulfilling the criteria listed in bullet-points i to iii in Section 3.1), and number of new redshifts obtained in our spectroscopic campaign (with quality flag ≥ -1 , c.f. Section 3.3).

Field	No. lit. z in HI-range	No. HI galaxies	No. WHT targets	No. WHT z in HI-range
A963	161	119	853	261
A2192	67	37	612	251

We obtained the data in 2 runs (April and June 2011) during 5 dark nights in total. In this time, we were able to observe 12 fiber configurations, each containing ~ 80 galaxies. The targeted galaxies were divided into different configurations (see Table 2) depending on their luminosities: for each field we created 3 bright and 3 faint configurations. For the bright ones, the exposure times were chosen to be one hour and for the faint ones 3 hours, in order to recover a signal-to-noise $\gtrsim 10$, although in practice, we extended the exposure times when possible. We tried to maximize the number of

fibers allocated on galaxies but also placed typically 20-30 fibers on the sky, for sky subtraction purposes.

As explained in Section 3.1, we prioritized our targets according to their HI content, and previous observations. Although we did not target the same galaxy more than once, in some cases, the software that allocates fibers to coordinates in the sky (AF2.CONFIGURE) used fibers, that could not be allocated to a new galaxy, to target galaxies previously observed in another configuration. For this reason, we have a few dozen galaxies with repeated observations (in different configurations, and sometimes in different runs), which were helpful for characterizing our redshift errors and the quality of our data.

The data were reduced using the new AF2 data reduction pipeline². We started using the pipeline before the final version was released, and hence helped testing the pipeline. Our final spectra however were reduced with the latest (final) version. To control the quality of our final reduction, we compared the final product with (a subsample of) the same spectra reduced with IRAF (using the IRAF package *dofiber*), coming to the conclusion that the pipeline performs well, and that it is significantly faster and more efficient than *dofiber*.

² For description and download of the pipeline visit: <http://www.ing.iac.es/Astronomy/instruments/af2/pipeline.html>

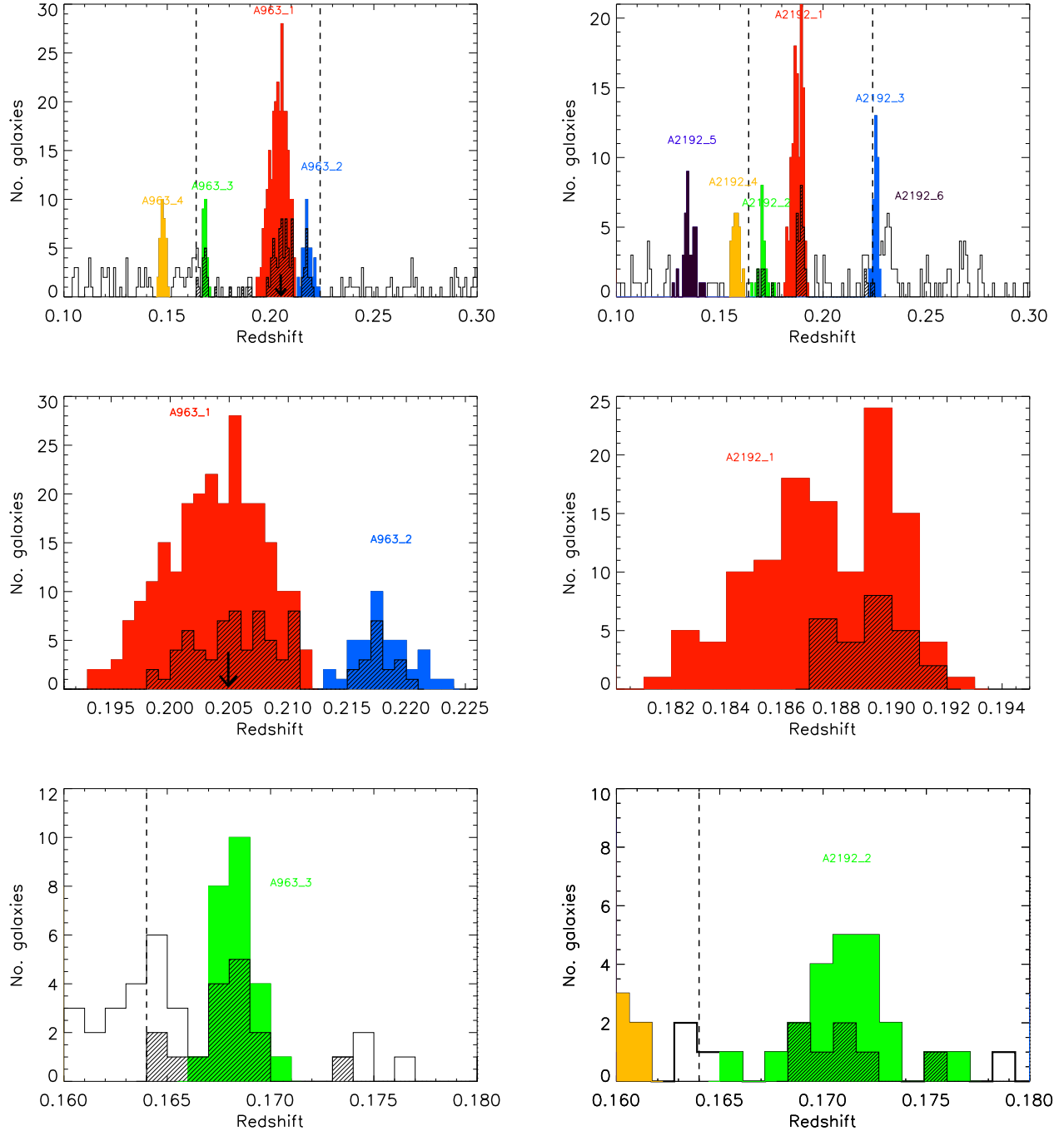


Figure 5. Redshift histograms for A963 (left) and A2192 (right). The top panels show the full redshift range of BUDHIES (The limits of the HI survey are indicated with vertical dashed lines), the middle panels a zoom in on the main clusters, and bottom panels additional groups. The open histograms correspond to the distribution of all galaxies with a redshift (of all qualities). The filled-dashed histograms show the HI-detected galaxies for reference, although we note that these will be fully analysed in a subsequent paper. The different structures identified are represented in different colours, as described by the labels. In the case of A963_1, the redshift of its brightest cluster galaxy is indicated with an arrow.

The pipeline is written in IDL and is able to perform full data reduction, including fiber to fiber sensitivity corrections and optimal extraction of the individual spectra. The first steps of the pipeline include master bias correction, tracing of the fibers, flat-field correction, and masking of bad pixels

in the science data. Twilight sky flats were used to define the apertures and trace the spectra on the CCD, and to perform the flat-field correction. An optimal extraction algorithm is used for extracting the spectra. The software accounts for wing emission from adjacent fibers.

As for the wavelength calibration, the software selects an arc lamp spectrum from a fiber near the centre of the chip. The user is then prompted to identify the principle arc lines (between 10 and 12 in our case). Other significant lines are automatically identified and then a dispersion solution is found using a polynomial fit. Once the user is satisfied, the dispersion solution is propagated to the rest of the fibers. Typically, the fits yielded an rms scatter of 0.03 Å.

Because not all fibers have the same throughput, we scaled the final spectra according to an estimation of the throughput in each fiber that the pipeline estimates from the master flat.

A master sky spectrum was also derived for each exposure by combining the spectra (using the median) of the 20-30 individual fibers assigned to the sky. The median is then subtracted from each science spectrum.

Finally, the multiple exposures in each pointing were combined (after extraction) with cosmic rays being removed.

Figure 4 shows example reduced spectra, and Table 1 summarizes the target selection and the outcome of our spectroscopic campaign.

3.3 Galaxy Redshifts and EW[OII]

Spectroscopic galaxy redshifts were measured using emission lines where possible (typically the [OII]3727Å line), or the most prominent absorption lines (e.g. Ca H&K lines at 3934Å and 3968Å), as shown in Figure 4. The redshifts were manually assigned a quality flag of 1 (reliable redshifts), -1 (reliable redshifts but with larger uncertainties) or -2 (unreliable redshifts). Over half (60%) of the measured redshifts are of high quality (≥ -1). Some of the objects however, have an unreliable redshift (10%), or in some cases no redshift could be determined (30%). A table containing all the measured redshifts (and EW[OII]) is available in the electronic version of the paper (see Table C1 for a shorter version).

In total, we measured 512 new reliable (quality ≥ -1) redshifts in A2192 and A963. The redshift distributions for the surveyed volumes are shown in the top panels of Figure 5. Note that the redshift distribution of the HI-detected galaxies is overplotted in the histograms for reference, although the complete analysis of the distribution and properties of the HI-detected galaxies will be presented in subsequent papers. We refer to Jaffé et al. (2012) for first results on the HI distribution in A2192's main cluster.

We estimate the typical redshift error from galaxies that have been observed more than once (i.e. in more than one configuration) and we get an uncertainty of ± 0.0003 . We further cross-checked our redshift measurements with previous spectroscopic observations, available for a substantial number of galaxies in our sample and confirmed the quality of our redshift measurements.

In addition to the redshifts, we also measured rest-frame equivalent widths (EW) of the [OII]3727Å line, which will be used as a proxy for ongoing star formation in forthcoming papers. The EW[OII] values are listed in Table C1 for future reference.

3.4 Completeness and success rate

For our analysis in this and other forthcoming papers, it is very important to know the spectroscopic completeness,

as it will affect local densities, or any magnitude-dependent analysis (e.g. the different galaxy population fractions inside clusters).

First, we assessed the completeness as a function of magnitude (m) as follows:

$$C(m) = \frac{N_z}{N_{\text{tar}}(m)} \quad (1)$$

where, N_z is the number of galaxies with reliable redshift and N_{tar} is the total number of targeted galaxies for spectroscopy (i.e. all the galaxies in our photometry that lie inside the CMD box and are inside the unvignetted field-of-view of the WHT, c.f. Section 3).

The success rate, i.e. the fraction of galaxies with trusted redshift determination with respect to the total number of galaxies observed, is defined as:

$$SR(m) = \frac{N_z}{N_{\text{obs}}}(m) \quad (2)$$

where, N_{obs} is the number of galaxies spectroscopically observed.

This assessment of the completeness only gives a general idea of our completeness limits, as shown in Figure 6. In the upper panel, the magnitude distribution of the targeted, observed and reliable-redshift samples are shown, and in the lower panels the completeness and success rate as a function of magnitude are plotted. This plot shows that our sample is complete to $> 40\%$ almost across all magnitudes.

To accurately correct for completeness, we further quantified possible changes with colour and spatial distribution. We did this by computing the completeness in colour-magnitude bins and in $\alpha - \delta$ bins. Colour bins were ~ 0.5 magnitudes wide, and geometrical bins were $\sim 0.3^\circ$. The R -band magnitude bins were larger towards the brighter end to allow a similar number of galaxies in each colour-magnitude bin. The geometrical effects could be caused by fiber collisions in the cluster centre, where there is more crowding. The effect is expected to be small as we had several configurations of the same cluster. Nevertheless, a geometrical completeness (C_{geo}) was calculated after applying the colour-magnitude completeness correction (C_{CM}).

The colour-magnitude and geometrical completeness functions will be applied to the spectroscopic sample in the following papers of the series to calculate fractions of a given galaxy population (e.g. the fraction of HI-detected galaxies as a function of environment). This can be achieved by weighting each galaxy by $C_{\text{CM}} + C_{\text{geo}}$, where $\Sigma(C_{\text{CM}}) = N_{\text{tar}}$ and $\Sigma(C_{\text{geo}}) = 1$.

4 VELOCITY DISPERSIONS AND CLUSTER/GROUP MEMBERSHIP

To identify the main clusters and other structures in the fields of A963 and A2192, we used the following approach.

Using galaxies with high quality redshifts (≥ -1), we constructed redshift histograms and identified (by eye) possible galaxy overdensities. This is shown in the top panels of Figure 5, where all the identified structures are highlighted.

Following the approach of Beers, Flynn & Gebhardt

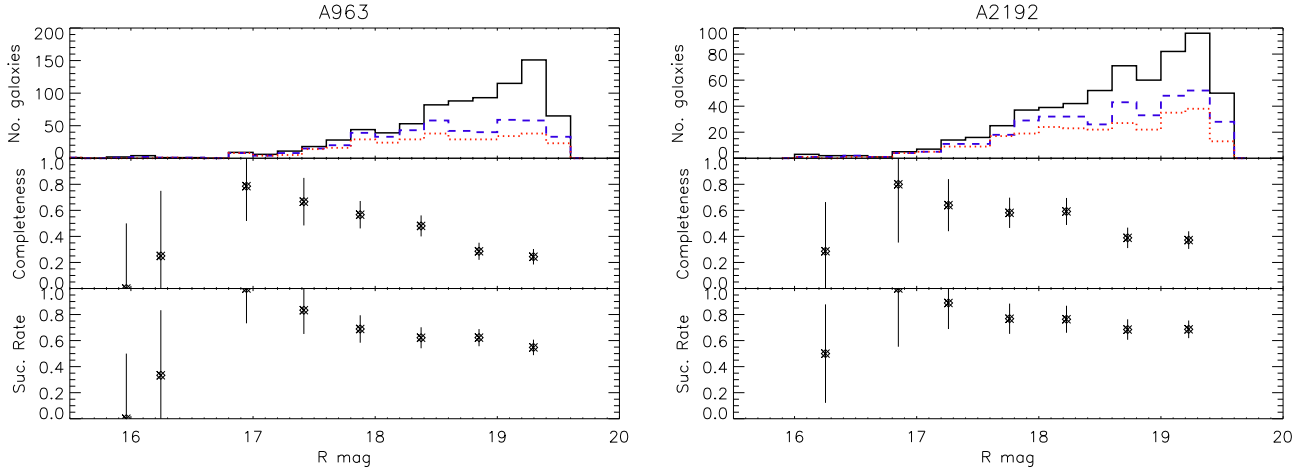


Figure 6. The top panels of this figure show the magnitude distribution of the targeted sample (solid histogram), in addition to the observed targets (blue dashed histogram) and the observed targets with trusted redshifts (red dotted histogram) for A963 (left) and A2192 (right). The middle and bottom panels show the completeness and success rate (respectively) as a function of magnitude. All the available redshifts were used to compute the completeness.

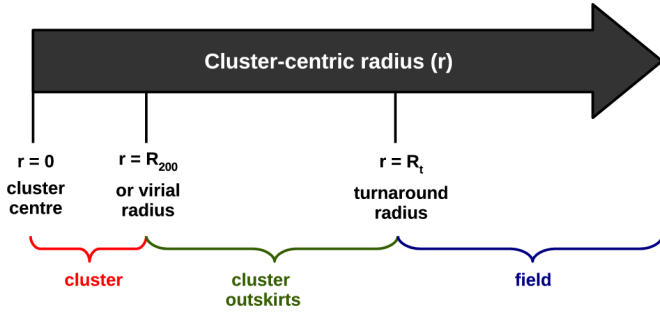


Figure 7. Illustrative schema of our environment definition criteria. The arrow represents the cluster-centric radius, going from the cluster's central region ($0 < r < R_{200}$), passing through the cluster outskirts ($R_{200} < r < R_t$), and ending in the field ($r > R_t$).

(1990), we computed the cluster velocity dispersion and central redshift in each case. Equation 3 shows the definition of the peculiar velocity of a galaxy with redshift z in the rest frame of a cluster with redshift z_{cl} . This equation is valid to first order for $v \ll c$ (Harrison 1974; Carlberg et al. 1996). The velocity dispersion of the cluster (σ_{cl}) is then defined as the dispersion of the v values for the cluster members. This value is related to the observed velocity dispersion (σ_{obs}), as shown in Equation 4.

$$v = c \frac{z - z_{cl}}{1 + z_{cl}} \quad (3)$$

$$\sigma_{cl} = \frac{\sigma_{obs}}{1 + z_{cl}} \quad (4)$$

Because the velocity dispersion of a cluster is a proxy for cluster mass (see Finn et al. 2005), we use it to distinguish galaxy clusters from less massive groups. Although there is no strict velocity dispersion cutoff for separating groups

from poor clusters, in our environmental definition, we adopt a threshold value of 500 km s^{-1} , following Mulchaey (2000).

We further calculated R_{200} , the radius delimiting a sphere with a mean density equal to 200 times the critical density³, as in Poggianti et al. (2006):

$$R_{200} = 1.73 \frac{\sigma_{cl}}{1000 \text{ km s}^{-1}} \frac{1}{\sqrt{\Omega_{\Lambda} + \Omega_0(1 + z_{cl})^3}} h^{-1} \text{ Mpc} \quad (5)$$

To carefully distinguish between environments, we classify galaxies within or around a cluster or group in the following categories: cluster, cluster outskirts and field. For this, we make use of R_{200} and the so-called turnaround radius, R_t , that separates the infall region and the field. Following the work of Rines & Diaferio (2006), we assume that $R_t/R_{200} = 4.57$. We define *cluster* galaxies to be inside R_{200} , *outskirt* galaxies to lie between R_{200} and R_t , and *field* galaxies to be beyond R_t , as shown schematically in Figure 7.

Table 4 lists the σ_{cl} , R_{200} , central redshift and number of members for each structure found inside the HI survey's volume. Table A1 lists other structures identified outside the studied redshift range.

5 CLUSTER SUBSTRUCTURE

Numerical dark matter simulations of galaxy groups and clusters in a Λ CDM universe predict that a significant fraction (30%) of all systems should contain substructure (Knebe & Müller 2000). Because it reflects the dynamical state of a cluster, it is thus important to quantify the incidence of substructure, and to take it into account when studying galaxy properties as a function of environment. In Jaffé et al. (2012) we showed that A2192_1 is a cluster with very clear spatially and dynamically distinct substructures inside it. Our analysis suggested that it is a cluster that is in the process of forming.

³ R_{200} is commonly used as an equivalent of virial radius.

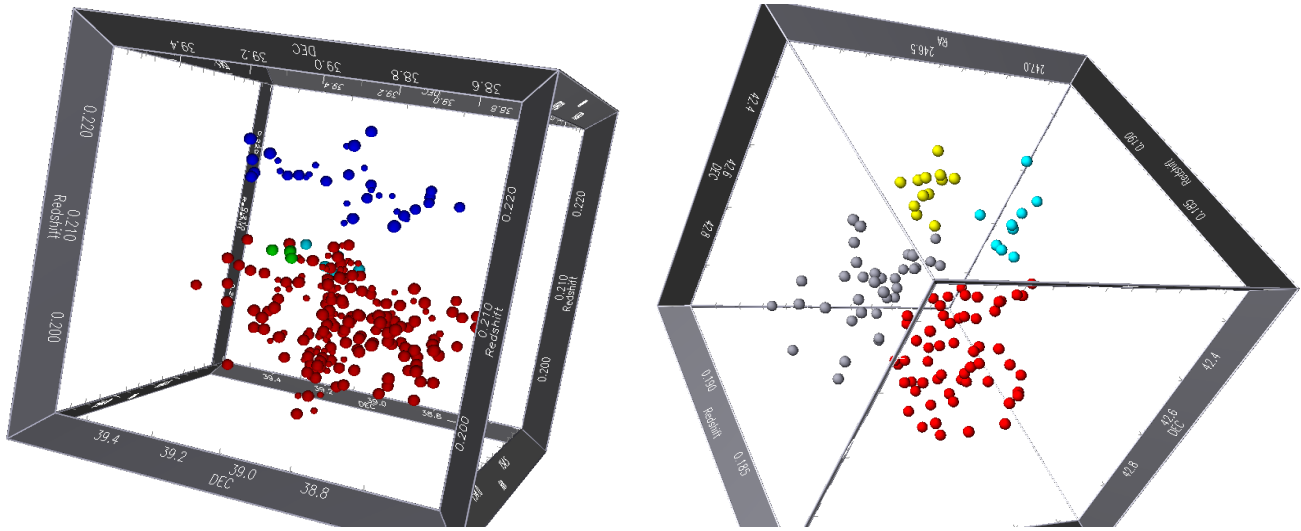


Figure 8. 3D visualization of the distribution of galaxies in the main clusters. The galaxies are plotted in right ascension vs. declination vs. redshift. The left panel shows the massive cluster A963.1 (red), its substructures A963.1a and A963.1b (coloured in turquoise and green respectively, see Sections 5.2 and 6), and A963.2 (blue). Smaller symbols represent the galaxies with less reliable redshifts (including the cluster members from Lavery & Henry 1994). The right-hand side shows A2192.1 split into its substructures: A2192.1a (red), A2192.1b (gray), A2192.1c (turquoise), and A2192.1d (yellow). This figure is three-dimensionally interactive in the online version of the paper, allowing the reader to change the magnification and viewing angle. The plots were constructed with the S2PLOT programming library (Barnes et al. 2006). A recent version of Adobe Acrobat Reader is required to display the content of this figure correctly. Click on each panel to activate the figure. Movies of the animated figures can also be found on the BUDHIES website <http://www.astro.rug.nl/budhies/>, or in the online supplementary material.

There are many ways to detect substructure in clusters. A first approach is to study the Gaussianity of the velocity distribution. For example, from Figure 5 (middle-right panel) alone we can note a double-peak in A2192.1 that already suggests the presence of substructure. However, velocity information alone does not necessarily reveal substructures within a cluster. Instead, it is important to look for deviations in the spatial and velocity distribution of galaxies simultaneously.

5.1 A Three-dimensional view of the clusters

To study and identify the presence of substructure within the clusters, we looked for deviations in the spatial and/or velocity distribution of galaxies in each structure. One way to do this is to visually inspect 3-dimensional (3D) maps of the galaxies' α , δ and redshift space. Figure 8 shows the 3D maps, centered on the richest structures in the survey.

From this exercise, we can clearly see galaxy overdensities that are well separated in space and velocity. The most striking case is that of A2192.1, because it shows clearly four separated substructures in space and velocity (coloured in red, gray, yellow and turquoise). This cluster has been thoroughly analyzed in Jaffé et al. (2012), where we have also studied the distribution of HI-detected galaxies around the substructures. A963.1 on the other hand presents a different case. It is populated by more galaxies than A2192.1 and their distribution in 3D space is more homogeneous. A clear feature is the “finger” of galaxies along the z -direction, that represents the cluster core, but in the 3D distribution of this cluster there are no easily distinguishable substructures. In the following (Section 5.2) we will complement the 3D

view of the clusters with statistical substructure tests, and in Section 6 we summarize the results of our environment analysis.

5.2 The Dressler-Shectman test

To further test the presence of substructure in the clusters and groups, we carried out the Dressler-Shectman (DS) test (Dressler & Shectman 1988), that compares the *local* velocity and velocity dispersion for each galaxy with the *global* values. To do this, we define $(\bar{v}_{cl}$ and σ_{cl}) as the mean velocity and velocity dispersion of the cluster/group, which is assumed to have N_{mem} galaxies. Then, for each galaxy i , we select a subsample of galaxies containing the galaxy i , plus its nearest N_{nn} neighbors, and compute their mean velocity \bar{v}_{local}^i and velocity dispersion σ_{local}^i . From these, we compute the individual galaxy deviations δ_i , following:

$$\delta_i^2 = \left(\frac{N_{nn} + 1}{\sigma_{cl}^2} \right) \left[(\bar{v}_{local}^i - \bar{v}_{cl})^2 + (\sigma_{local}^i - \sigma_{cl})^2 \right] \quad (6)$$

We used $N_{nn} = 10$ in our clusters and $N_{nn} = \sqrt{N_{mem}}$ in groups with less than 20 members.

We performed two DS statistical tests:

(i) The first is the “critical value” method, in which a Δ -value is computed by:

$$\Delta = \sum_i \delta_i \quad (7)$$

Then, a system is considered to have substructure if $\Delta/N_{mem} > 1$.

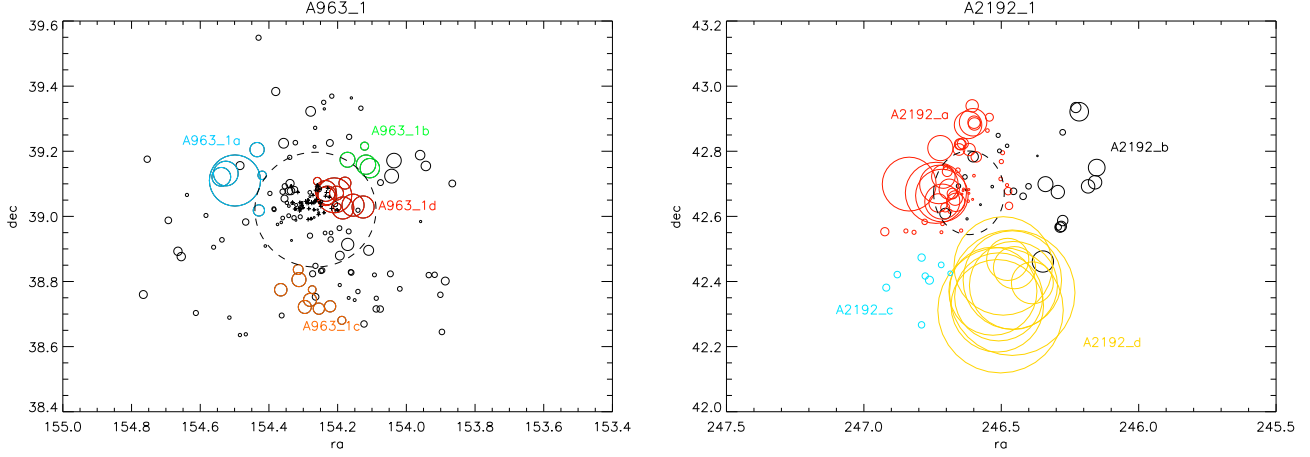


Figure 9. The Dressler & Shectman (1988) “bubble-plot” for the two main clusters in our sample. Galaxies are plotted with circles with a diameter that scales with $\exp(\delta_i)$. Colours indicate substructures identified. Dashed circles indicate the R_{200} radius of the clusters. Only galaxies with good quality redshifts inside the CMD box were considered. The crosses in the the centre of A963 (left panel) correspond to additional cluster members from Lavery & Henry (1994, and private communication). The “bubble-plots” for the other clusters/groups in our sample are shown in Appendix B.

Table 3. Results from the Dressler-Schectman test for substructure. Higher values of $\Delta_{\text{obs}}/N_{\text{mem}}$ indicate more likeliness to host substructure. Inversly, lower values of P indicate a higher probability that the cluster/group has significant substructure. We adopt $P \lesssim 0.01$ to identify the cluster/groups with significant substructure.

Name of structure	N_{mem}	$\Delta_{\text{obs}}/N_{\text{mem}}$	P
A963_1	140	1.44	0.005
A963_2	21	1.65	0.27
A963_3	16	1.43	0.5
A2192_1	103	1.96	<0.001
A2192_2	15	1.91	0.015
A2192_3	11	1.79	0.011

(ii) The second method uses probabilities (P) rather than critical values. The P -values are computed by comparing the Δ -value to “shuffled” Δ -values, which are computed by randomly shuffling the observed velocities and reassigning these values to the member positions (i.e. Monte Carlo shuffling). The P -values are given by:

$$P = \sum (\Delta_{\text{shuffle}} > \Delta_{\text{obs}}/N_{\text{shuffle}}) \quad (8)$$

Where Δ_{shuffle} and Δ_{obs} are computed following Equation 7 and N_{shuffle} is the number of Monte Carlo shuffles performed, typically around 5000. A system is then considered to host substructure if it has a very small P -value ($\lesssim 0.01$), as it is unlikely to obtain Δ_{obs} randomly.

We applied both methods to the spectroscopic sample (see Table 3), but focus on the P values to identify cluster/groups with substructure. We found that the main clusters, A2192_1 and A963_1 have very small P values ($\lesssim 0.01$), which strongly suggests that they have significant substructure. The other clusters and groups have smaller, although

non negligible, probabilities of hosting substructure (i.e. higher P values).

Figures 9 and B1 further show the Dressler & Shectman (1988) “bubble-plots” for each cluster/group in our sample. In these plots, each galaxy is marked by a circle with a size proportional to $\exp(\delta_i)$, so that galaxies with kinematics deviating significantly from the kinematics of the cluster can be easily identified. In our study, we considered significant deviations those with $\exp(\delta_i) \gtrsim 6$. In these figures the spectroscopic sample defined in Section 3.1 was utilized. Only high quality redshifts (≥ -1) were considered, which excludes literature data from Lavery & Henry (1994, and private communication).

We used the “bubble-plots” to confirm the substructures found in Figure 8 for A2192_1 (see also Jaffé et al. 2012) and further identify less obvious substructures in A963_1. First, we selected groups of galaxies with bigger circles in the bubble-plots (i.e. significant kinematic deviation from the cluster) in a similar manner as in Bravo-Alfaro et al. (2009). In addition to this, once a substructure (i.e. a group of galaxies with similar-size circles) was identified, we examined the velocity distribution and discarded clear outliers. In this way we can be more certain that the substructures we identify are not only spatially concentrated, but also have consistent velocities. For this reason, the substructures coloured in Figure 9 may have similar-sized uncoloured circles near them that are not considered part of the substructure (see for example the case of A963_1b). This process confirmed the reality of the four substructures found in A2192_1, and identified two poor groups with consistent velocities in the outskirts of A963_1 (A963_1a and A963_1b, fully discussed in Section 6).

Overall, the Dressler-Shectman test revealed that the substructure in A963_1 is more sparsely distributed around the cluster outskirts (bigger -black and coloured- circles outside R_{200} in the left-hand side of Figure 9), whilst for A2192_1, the substructures found (coloured circles in the right-hand side of Figure 9) are very distinct, as we had

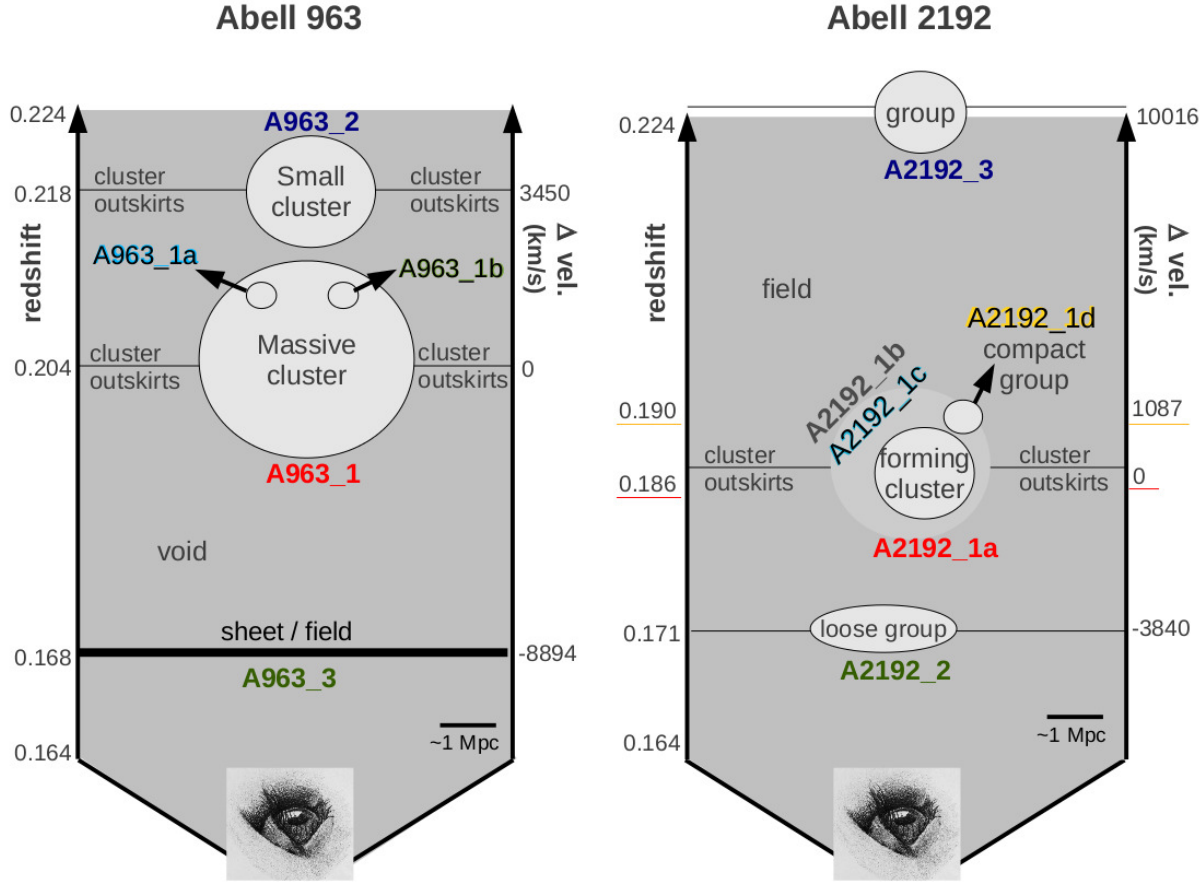


Figure 10. Schematic view of the different environments defined in this paper. The eyes looking upwards at the bottom of each panel indicate the line-of-sight. As a consequence redshift increases vertically (left axis). Only the redshift range of the HI observations is shown. Additionally, the axes on the right of each panel indicate the velocity difference ($\Delta \text{vel.}$) between each structure and the main cluster (A963.1 in the left panel and A2192.1a in the right panel). The sizes of the clusters have been roughly scaled for comparison, in accordance with the 1 Mpc scale (at the main cluster’s redshift) shown at the bottom-right (black solid line) of each panel.

found already in Figure 8 and Jaffé et al. (2012) from the 3D distribution of the galaxies.

6 SUMMARY OF THE STRUCTURES

Our environmental analysis (c.f. Sections 5.2 and 5.1) yielded a wide range of environments in the two surveyed volumes. Specifically, we identified two clusters, one in each field, containing well-defined substructure within them. Together with these clusters, we found several foreground and background cluster/groups⁴ in the redshift range $0.164 \leq z \leq 0.224$, as illustrated in Figure 10. The main properties of the structures found are listed in Table 4.

In the following, we combine all our results to summarize the main characteristics of each structure.

- **A963_1:** is the richest and most massive cluster in the surveyed volumes. Consisting of 141 spectroscopically confirmed galaxies (with $R < 19.5$), it has a dynamical mass of

$1.1 \times 10^{15} h^{-1} M_{\odot}$ and a virial radius of $1.55 h^{-1} \text{Mpc}$ (both estimated from the measured $\sigma_{\text{cl}} = 993 \text{ km s}^{-1}$). A963.1 has previously been studied both in X-rays and using weak lensing (Allen et al. 2003; Smith et al. 2005). The cluster has been classified as “relaxed”, as it shows very regular and centrally concentrated X-ray and mass morphologies (on a central cD galaxy) (see Fig. 6 of Smith et al. 2005), which suggests a low level of substructure. Its total mass has been estimated to be $3.5 \pm 0.3 \times 10^{14} h^{-1} M_{\odot}$ from the lensing analysis, which is lower than our σ_{cl} -derived measure. Moreover, its total X-ray luminosity is $L_X = 3.4 \pm 1 \times 10^{44} h^{-2} \text{erg/s}$, and the X-ray estimated R_{200} is $1.2 \pm 0.1 h^{-1} \text{Mpc}$, which is also smaller than the dynamical value we measure ($= 1.55 h^{-1} \text{Mpc}$, see Table 4). Our analysis, combined with the X-ray observations, suggests that the “relaxed” part of the cluster is at its core, while the substructure dominates the outskirts.

The DS test in A963.1 yielded $\Delta/N_{\text{mem}} = 1.44$ and $P = 0.005$ (c.f. Table 3), which strongly indicates it has substructure. Figure 9 reveals a spread population of galaxies surrounding the cluster with evident velocity and spatial offsets from the cluster (see bigger -black and coloured- circles surrounding the cluster centre), suggesting it might be

⁴ As explained in Section 3.3, we separate clusters from groups using a threshold cluster velocity dispersion value of 500 km s^{-1} .

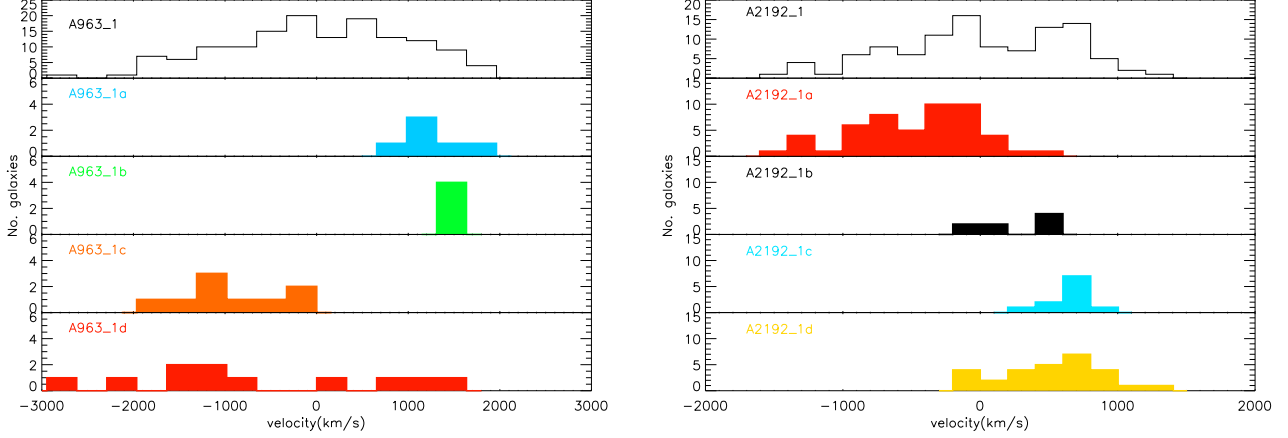


Figure 11. Velocity distribution of the substructures within A963.1 and A2192.1, identified in Figure 9. For reference, the velocity distribution of all the galaxies in A963.1 and A2192.1 respectively are shown at the top. In the other panels, the colours and labels are as in Figure 9. The spread in velocity of A963.1c and A963.1d suggests that they are not virialized galaxy groups, whilst the narrow velocity range of A963.1a and A963.1b strongly suggest the presence of a bound group of galaxies. In the case of the structures in A2192.1, they all have a clearly separated velocity distributions.

a population of infalling field galaxies. Moreover, there are 4 substructures (coloured and labeled in the figure) that could represent accreted galaxy groups in the process of destruction. This seems plausible given that they lie within the turnaround radius ($4.57 \times R_{200}$). To verify the reality of these groups, we inspected their velocity distributions, as shown in Figure 11. We find that only 2 groups, namely A963.1a and A963.1b have tight velocity distributions (at 1230 and 1548 km s^{-1} from the main cluster respectively), indicating they are likely bound groups. However, in A963.1c and A963.1d there is not a clear separation in the velocity space alone. In fact, their broad velocity distributions indicate that they are not gravitationally bound groups. We thus conclude that A963.1 is a cluster with significant substructure, including two poor groups at $\gtrsim R_{200}$, but dominated by a spread population of infalling galaxies in the cluster’s outskirts.

- **A963.2:** is a $1.4 \times 10^{14} h^{-1} M_{\odot}$ ($\sigma_{\text{cl}} = 507 \text{ km s}^{-1}$) cluster located at the same position in the sky as A963.1, but at slightly higher redshift. Although it is tempting to think that A963.2 is in the process of falling into A963.1, it is important to note that A963.2 lies outside the turnaround radius of the main cluster. In fact, A963.2 has a velocity difference of $\sim 3450 \text{ km s}^{-1}$ from A963.1’s centre (over 3 times the σ_{cl} of A963.1), so it is unlikely that these clusters are interacting.

The velocity distribution of this cluster resembles a Gaussian, although it also shows some hints of asymmetry. In particular, it shows a prominent and narrow velocity peak at the central velocity with a normal distribution underneath it. If this feature is real, it could be interpreted as a cosmic sheet at the peak’s redshift that contains an intermediate-size cluster. Moreover, the substructure analysis in A963.2 does not give strong evidence of substructure.

- **A963.3:** This family of galaxies with a narrow velocity distribution but very spread out in space, is likely to be a cosmic sheet and not a galaxy group. There is a very low probability that A963.3 contains substructure, supporting

the idea that this group is just a population of field galaxies at the same redshift.

- **A2192.1:** is a forming cluster with significant substructure. This cluster has been fully explored in Jaffé et al. (2012). In short, A2192.1 is composed by a $1.6 \times 10^{14} h^{-1} M_{\odot}$ ($\sigma_{\text{cl}} = 530 \text{ km s}^{-1}$) cluster, A2192.1a, which is the forming cluster itself that coincides with (weak) X-ray emission. Surrounding the cluster, we find a compact group, A2192.1d, and a scattered population of “field-like” galaxies A2192.1b and A2192.1c. As explained in Jaffé et al. (2012), A2192.1b and A2192.1c are “field-like” because they are spread in space and their galaxy population resembles that of the field. These substructures, although unlikely to be bound, are considered part of A2192.1 since they are well within the turnaround radius. Supporting our findings, the Dressler-Shectman “bubble-plot” (right-hand side of Figure 9) revealed the same substructures found in Figure 8 (see also Figure 2 of Jaffé et al. 2012).

In contrast with A963.1, A2192.1 has very weak X-ray emission. However, the existent emission coincides with a group of early-type galaxies at the core of A2192.1a. Moreover, the X-ray luminosity ($L_X \simeq 7 \times 10^{43} h^{-2} \text{ erg/s}$; Voges et al. 1999) is consistent with the derived dynamical mass.

- **A2192.2:** with a dynamical mass of $9.9 \times 10^{13} h^{-1} M_{\odot}$ ($\sigma_{\text{cl}} = 447 \text{ km s}^{-1}$), this galaxy group is clearly separated in velocity space from the others in the field. Although its mass is very similar to that of the low-mass cluster A963.2, A2192.2 has a σ_{cl} below our threshold limit, so we have classified it as a group. Moreover it is considerably spread in space and has substructure, which makes it a loose group.

- **A2192.3:** is a $4.21 \times 10^{13} h^{-1} M_{\odot}$ ($\sigma_{\text{cl}} = 340 \text{ km s}^{-1}$) group of galaxies with little substructure.

Table 4 lists the main characteristics of the structures described above. Other cluster/groups outside the surveyed volume, but identified by our spectroscopic campaign, are listed in Table A1 for completeness.

Table 4. Clusters, groups and other structures identified in the fields of A963 and A2192 inside the redshift range of the HI-observations. The columns indicate the field, structure, central redshift (z_c), number of members in the reduced sample (and -for the main clusters- number of members within R_{200}), cluster velocity dispersion, R_{200} , and comments.

Field	Name of structure	z_c	No. members ($R < 19.4\text{mag}$)	σ_{cl} (km s^{-1})	R_{200} (h^{-1}Mpc)	Remarks
A963	A963.1	0.2039	141 (67)	993 ± 56	1.55	Main cluster in A963
	A963.1a	0.2089	7	–	–	Small substructure in A963.1
	A963.1b	0.2103	4	–	–	Small substructure in A963.1
	A963.2	0.2178	21	507 ± 158	0.79	Intermediate-size cluster near A963.1
	A963.3	0.1682	15	–	–	Cosmic sheet, very narrow in z and spread in $\alpha - \delta$
	A963 field	$0.164 \leq z \leq 0.224$	30	–	–	Galaxies not belonging to any cluster/group
A2192	A2192.1	0.1876	103 (39)	645 ± 42	1.02	Main cluster in A2192 (see Jaffé et al. 2012)
	A2192.1a	0.1859	50	530 ± 56	0.84	Substructure of A2192.1
	A2192.1b	0.1898	29	–	–	“Field-like” substructure of A2192.1
	A2192.1c	0.1881	8	–	–	“Field-like” substructure of A2192.1
	A2192.1d	0.1902	11	161 ± 52	0.25	Compact group, substructure of A2192.1
	A2192.2	0.1707	17	477 ± 103	0.71	Loose group
	A2192.3*	0.2255	30	340 ± 71	0.53	Galaxy group
	A2192 field	$0.164 \leq z \leq 0.224$	20	–	–	Galaxies not belonging to any cluster/group

* This group spans a redshift range that exceeds the limit of the HI survey, and hence suffers from incompleteness.

7 CONCLUSIONS

With the WSRT, BUDHIES has detected HI in over 150 galaxies in and around 2 Abell clusters at $z \approx 0.2$ (Deshev et al. in preparation). As part of BUDHIES, we have also carried out spectroscopic observations of the galaxies in the two surveyed volumes with AF2+WYFFOS on the WHT. In this paper we provide details of the spectroscopic target selection, observations, and data reduction. The observations allowed us to measure many redshifts that mapped the cosmic large-scale structure in these volumes and thus characterize the environment of the HI-detected galaxies in the surveyed volume. We present data tables containing positions, redshifts, equivalent widths of the [OII] emission, and B - and R -band magnitudes for galaxies in the volumes.

The redshift distribution revealed several structures in each of the surveyed volume, ranging from massive clusters to small groups, cosmic sheets and voids. We further present an environment classification scheme in which we consider “cluster” galaxies those within R_{200} , “outskirts” the region between R_{200} and the turnaround radius, and “field” all the galaxies beyond the turnaround radius.

By performing detailed substructure tests, we find that both main clusters (A963.1 and A2192.1) show a high degree of substructure within their turnaround radii, suggesting they are actively accreting galaxies from smaller groups or the field population. In particular, A963.1 shows weaker evidence for group accretion, and stronger evidence for accretion of (originally) field galaxies that are well spread in space and velocity. On the contrary, A2192.1 has very distinct substructures, strongly implying that the cluster is in the process of forming from the accretion of galaxy groups. The other cluster/groups in the survey have less complex substructure.

The diversity of environments found in the surveyed volumes, together with the unprecedented multi-wavelength dataset, makes BUDHIES an ideal laboratory to study environmental dependent processes such as strangulation, tidal

and ram pressure stripping and the importance of group pre-processing in galaxy evolution.

ACKNOWLEDGMENTS

YLJ and BMP acknowledge financial support from ASI through contract I/099/10/0, and FONDECYT grant No. 3130476. This work was supported in part by the National Science Foundation under grant No. 1009476 to Columbia University. We are grateful for support from a Da Vinci Professorship at the Kapteyn Institute. We thank Richard Jackson and Ian Skillen for their support on the new AF2 pipeline, and Daniela Bettoni for useful discussions. YLJ is grateful to Graeme Candlish for assistance creating the 3D plots.

REFERENCES

- Abramson A., Kenney J. D. P., Crowl H. H., Chung A., van Gorkom J. H., Vollmer B., Schiminovich D., 2011, *AJ*, 141, 164
- Allen S. W., Schmidt R. W., Fabian A. C., Ebeling H., 2003, *MNRAS*, 342, 287
- Barnes D. G., Fluke C. J., Bourke P. D., Parry O. T., 2006, *PASA*, 23, 82
- Beers T. C., Flynn K., Gebhardt K., 1990, *AJ*, 100, 32
- Bell M. B., 2007, *ApJ*, 667, L129
- Bolzonella M., et al., 2010, *A&A*, 524, A76+
- Bravo-Alfaro H., Caretta C. A., Lobo C., Durret F., Scott T., 2009, *A&A*, 495, 379
- Bravo-Alfaro H., Cayatte V., van Gorkom J. H., Balkowski C., 2000, *AJ*, 119, 580
- Bravo-Alfaro H., Cayatte V., van Gorkom J. H., Balkowski C., 2001, *A&A*, 379, 347
- Butcher H., Oemler A., 1978, *ApJ*, 219, 18

- Butcher H., Wells D. C., Oemler Jr. A., 1983, *ApJS*, 52, 183
- Carlberg R. G., Yee H. K. C., Ellingson E., Abraham R., Gravel P., Morris S., Pritchet C. J., 1996, *ApJ*, 462, 32
- Cayatte V., van Gorkom J. H., Balkowski C., Kotanyi C., 1990, *AJ*, 100, 604
- Chung A., van Gorkom J. H., Kenney J. D. P., Crowl H., Vollmer B., 2009, *AJ*, 138, 1741
- Chung A., van Gorkom J. H., Kenney J. D. P., Vollmer B., 2007, *ApJ*, 659, L115
- Crowl H. H., Kenney J. D. P., van Gorkom J. H., Vollmer B., 2005, *AJ*, 130, 65
- De Lucia G., Weinmann S., Poggianti B. M., Aragón-Salamanca A., Zaritsky D., 2012, *MNRAS*, 423, 1277
- Desai V., Dalcanton J. J., Aragón-Salamanca A., Jablonka P., Poggianti B., Gogarten S. M., Simard L., Milvang-Jensen B., Rudnick G., Zaritsky D., Clowe D., Halliday C., Pelló R., Saglia R., White S., 2007, *ApJ*, 660, 1151
- Dressler A., 1980, *ApJ*, 236, 351
- Dressler A., Oemler Jr. A., Couch W. J., Smail I., Ellis R. S., Barger A., Butcher H., Poggianti B. M., Sharples R. M., 1997, *ApJ*, 490, 577
- Dressler A., Shectman S. A., 1988, *AJ*, 95, 985
- Ellingson E., Lin H., Yee H. K. C., Carlberg R. G., 2001, *ApJ*, 547, 609
- Fadda D., Biviano A., Marleau F. R., Storrie-Lombardi L. J., Durret F., 2008, *ApJ*, 672, L9
- Fasano G., Poggianti B. M., Couch W. J., Bettoni D., Kjærgaard P., Moles M., 2000, *ApJ*, 542, 673
- Finn R. A., Zaritsky D., McCarthy D. W., Poggianti B., Rudnick G., Halliday C., Milvang-Jensen B., Pelló R., Simard L., 2005, *ApJ*, 630, 206
- Freeland E., Stilp A., Wilcots E., 2009, *AJ*, 138, 295
- Giovanelli R., et al., 2005, *AJ*, 130, 2598
- Gómez P. L., et al., 2003, *ApJ*, 584, 210
- Haines C. P., Gargiulo A., La Barbera F., Mercurio A., Merluzzi P., Busarello G., 2007, *MNRAS*, 381, 7
- Harrison E. R., 1974, *ApJ*, 191, L51
- Hibbard J. E., van der Hulst J. M., Barnes J. E., Rich R. M., 2001, *AJ*, 122, 2969
- Jaffé Y. L., Aragón-Salamanca A., Kuntschner H., Bamford S., Hoyos C., De Lucia G., Halliday C., Milvang-Jensen B., Poggianti B., Rudnick G., Saglia R. P., Sanchez-Blazquez P., Zaritsky D., 2011, *MNRAS*, 417, 1996
- Jaffé Y. L., Poggianti B. M., Verheijen M. A. W., Deshev B. Z., van Gorkom J. H., 2012, *ApJ*, 756, L28
- Kapferer W., Sluka C., Schindler S., Ferrari C., Ziegler B., 2009, *A&A*, 499, 87
- Kauffmann G., Colberg J. M., Diaferio A., White S. D. M., 1999, *MNRAS*, 307, 529
- Kenney J. D. P., van Gorkom J. H., Vollmer B., 2004, *AJ*, 127, 3361
- Kern K. M., Kilborn V. A., Forbes D. A., Koribalski B., 2008, *MNRAS*, 384, 305
- Knebe A., Müller V., 2000, *A&A*, 354, 761
- Kodama T., Bower R. G., 2001, *MNRAS*, 321, 18
- Lavery R. J., Henry J. P., 1994, *ApJ*, 426, 524
- Lewis I., et al., 2002, *MNRAS*, 334, 673
- Mahajan S., Raychaudhury S., Pimblet K. A., 2012, *MNRAS*, 427, 1252
- Meyer M. J., et al., 2004, *MNRAS*, 350, 1195
- Mulchaey J. S., 2000, *ARA&A*, 38, 289
- Oesch P. A., et al., 2010, *ApJ*, 714, L47
- Poggianti B. M., et al., 2006, *ApJ*, 642, 188
- Poggianti B. M., Smail I., Dressler A., Couch W. J., Barger A. J., Butcher H., Ellis R. S., Oemler A. J., 1999, *ApJ*, 518, 576
- Poggianti B. M., van Gorkom J. H., 2001, in J. E. Hibbard, M. Rupen, & J. H. van Gorkom ed., *Gas and Galaxy Evolution Vol. 240 of Astronomical Society of the Pacific Conference Series, Environmental Effects on Gas and Galaxy Evolution in Clusters*. p. 599
- Porter S. C., Raychaudhury S., Pimblet K. A., Drinkwater M. J., 2008, *MNRAS*, 388, 1152
- Rines K., Diaferio A., 2006, *AJ*, 132, 1275
- Roediger E., 2009, *Astronomische Nachrichten*, 330, 888
- Roychowdhury S., Chengalur J. N., Chiboucas K., Karachentsev I. D., Tully R. B., Kaisin S. S., 2012, *MNRAS*, 426, 665
- Scott T. C., Bravo-Alfaro H., Brinks E., Caretta C. A., Cortese L., Boselli A., Hardcastle M. J., Croston J. H., Plauchu I., 2010, *MNRAS*, 403, 1175
- Scott T. C., Cortese L., Brinks E., Bravo-Alfaro H., Auld R., Minchin R., 2012, *MNRAS*, 419, L19
- Smith G. P., Kneib J.-P., Smail I., Mazzotta P., Ebeling H., Czoske O., 2005, *MNRAS*, 359, 417
- Tonnesen S., Bryan G. L., 2009, *ApJ*, 694, 789
- Treu T., Ellis R. S., Kneib J., Dressler A., Smail I., Czoske O., Oemler A., Natarajan P., 2003, *ApJ*, 591, 53
- van der Hulst J. M., 1979, *A&A*, 75, 97
- van Dokkum P. G., Franx M., Kelson D. D., Illingworth G. D., Fisher D., Fabricant D., 1998, *ApJ*, 500, 714
- Verdes-Montenegro L., Yun M. S., Williams B. A., Huchtmeier W. K., Del Olmo A., Perea J., 2001, *A&A*, 377, 812
- Verheijen M., van Gorkom J. H., Szomoru A., Dwarakanath K. S., Poggianti B. M., Schiminovich D., 2007, *ApJ*, 668, L9
- Voges W., et al., 1999, *A&A*, 349, 389
- Vollmer B., 2003, *A&A*, 398, 525
- Vulcani B., Poggianti B. M., Finn R. A., Rudnick G., Desai V., Bamford S., 2010, *ApJ*, 710, L1
- Wilman D. J., Oemler Jr. A., Mulchaey J. S., McGee S. L., Balogh M. L., Bower R. G., 2009, *ApJ*, 692, 298

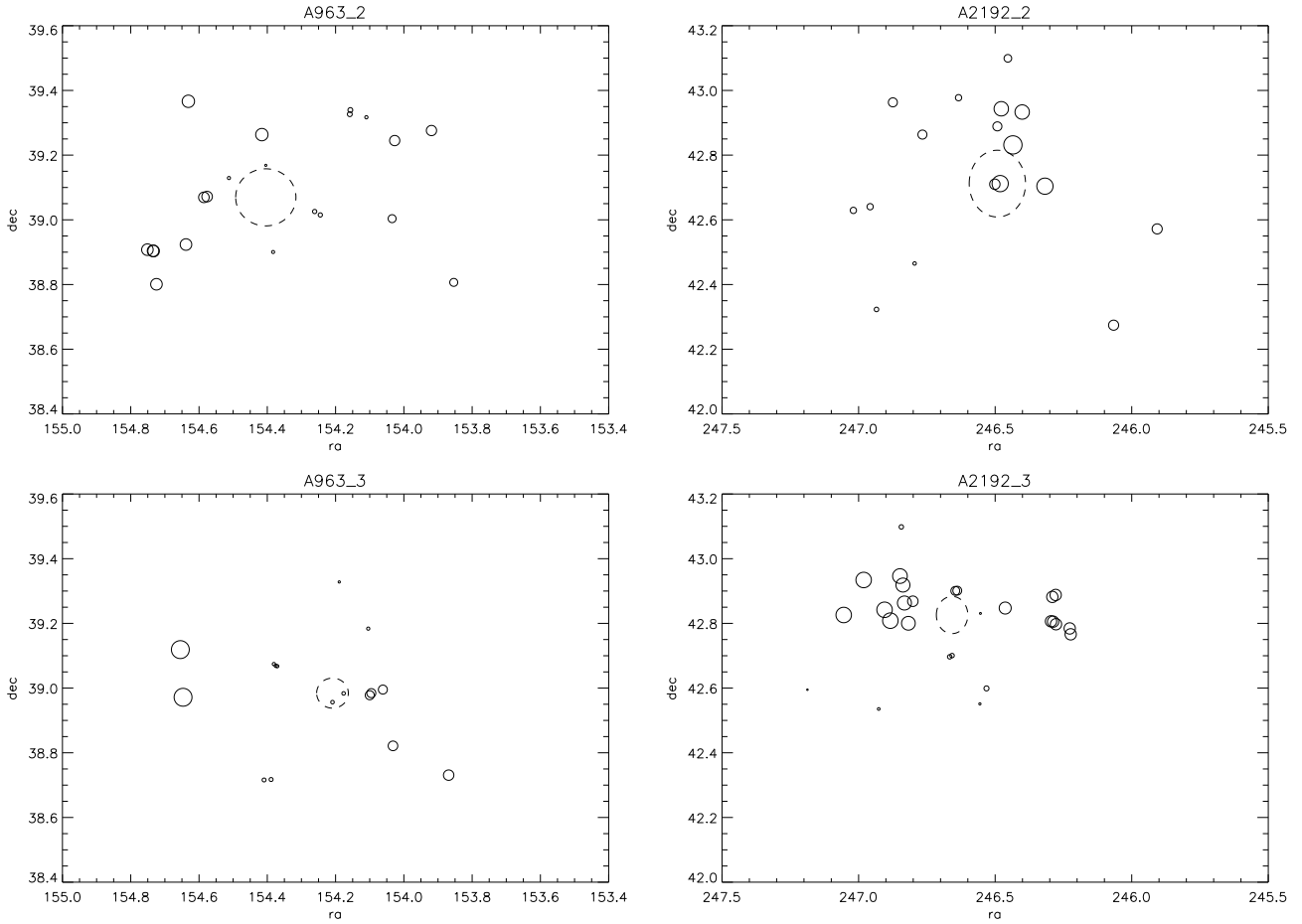
APPENDIX A: OTHER CLUSTER/GROUPS OUTSIDE THE SURVEYED VOLUME

In Table 4 we presented the main characteristics of the cluster/groups found in the BUDHIES volume. For completeness and future reference we show here a list of other structures identified by our spectroscopic campaign outside the redshift range of the HI survey ($0.164 \leq z \leq 0.224$).

APPENDIX B: THE DRESSLER-SHECTMAN TEST: BUBBLE PLOTS

Table A1. Clusters, groups and other structures identified in the fields of A963 and A2192 outside the redshift range of the HI-observations.

Field	Name of structure	z_c	No. members ($R < 19.4\text{mag}$)	σ_{cl} (km s^{-1})	R_{200} ($h^{-1} \text{ Mpc}$)	Remarks
A963	A963_4	0.1478	24	290 ± 53	0.47	Sparse in α and δ
A2192	A2192_4	0.1581	26	454 ± 64	0.73	Well-defined group.
	A2192_5	0.1348	35	717 ± 91	1.16	Scattered, double peaked in z
	A2192_6	0.2319	26	579 ± 92	0.89	“companion” of A2192_3

**Figure B1.** Figure 9 showed the Dressler & Shectman (1988) “bubble-plot” for the two main clusters in our sample. We show here the remaining cluster/groups. Galaxies are plotted with circles with a diameter that scales with $\exp(\delta_i)$. Dashed circles indicate the R_{200} radius of the clusters. Only galaxies with good quality redshifts were considered.

APPENDIX C: SPECTROSCOPIC CATALOGUE

In the following, we show an example 10 rows of the spectroscopic catalogue associated with this paper.

Table C1. This table contains the optical information for the galaxies observed with the WHT for which a redshift was obtained. Only 10 example rows are shown here. The full table is available in the online version of the paper. The ID is preceded by “IJ” and contains the right ascension and declination of the INT photometry in hms and dms format. The redshift quality ranges from 1 to -2, only redshifts quality ≥ -1 are to be trusted. The type of spectra is also indicated: “em” stands for emission-line spectra, “ab” for absorption, “em+ab” means that there are both types of features clearly visible, and “nan” corresponds to galaxies with unclear spectral features.

Field	ID	R mag	B mag	redshift	redshift quality	type of spectra	EW[OII]
A963	IJ101527.90+390603.6	18.67	20.03	0.2054	1	em+ab	14.28
A963	IJ101544.32+384910.9	19.99	20.78	0.2064	1	em/ab	11.1
A963	IJ101532.79+384805.1	18.45	20.71	0.2060	1	ab	--
A963	IJ101659.58+384956.2	18.78	20.82	0.2066	-1	ab	--
A963	IJ101721.29+390602.5	18.47	20.35	0.1993	1	nan	--
A963	IJ101701.54+390009.3	19.77	20.85	0.1650	1	em	57.22
A963	IJ101534.81+390912.0	18.20	20.42	0.1749	1	ab	--
A2192	IJ162431.50+424621.7	18.29	19.93	0.2612	1	ab	--
A2192	IJ162436.20+424111.7	19.97	20.91	0.1427	-2	ab	--
A2192	IJ162658.84+421557.1	19.34	21.20	0.1783	-1	ab	--